FREIE UNIVERSITÄT BERLIN

An adaptive Newton multigrid method for a model of marine ice sheets

Guillaume Jouvet[1a], Carsten Gräser[a,b]

Preprint A /01/2012

FACHBEREICH MATHEMATIK UND INFORMATIK

SERIE A • MATHEMATIK

An adaptive Newton multigrid method for a model of marine ice sheets

Guillaume Jouvet[1a], Carsten Gräser[a,b]

[a] *Department of Mathematics and Computer Science, Freie Universität Berlin, Berlin, Germany*
[b] *DFG Reseach Center Matheon, Berlin, Germany*

Abstract

In this paper, we consider a model for the time evolution of marine ice sheets. This model combines the Shallow Ice Approximation (SIA) for the ice deformation, the Shallow Shelf Approximation (SSA) for the basal sliding and the mass conservation principle. At each time step, we solve a generalized p-Laplace minimization-type problem with obstacle (SIA), a vectorial p-Laplace minimization-type problem (SSA) and a transport equation (mass conservation). The two minimization problems are solved using a truncated nonsmooth Newton multigrid method while the transport equation is solved using a vertex-centred finite volume method. Our approach is combined to a mesh adaptive refinement procedure to face the large gradients of the solution that are expected close to the grounding line which separates the ice sheet and the ice shelf. As applications, we present some simulations of the marine ice sheet model intercomparison project MISMIP in two and three space dimensions. In particular, we test the ability of our model to reproduce a reversible grounding line after being perturbed in model parameters.

1. Introduction

Warming in recent decades has caused a number of worldwide ice sheets to shrink substantially. As an example, the melting of Antarctic ice sheets has increased the global sea-level by ~ 0.4 millimetres per year during 2002–2005 [37]. Most of this mass loss came from the West Antarctic Ice Sheet (WAIS) [22]. The specificity of the WAIS is that most of its bedrock is located below the sea-level. Currently, only around one fourth of the WAIS is floating. However, this ratio might increase if the layer of ice gets thinner. In such condition, the Grounding Line (GL), that separates the grounded ice sheet and the floating ice shelf, might retreat by thousands of kilometres. Moreover, GLs are well-known to control the stability of marine ice sheets since they are unstable over upward-sloping bed [34]. Therefore, a small change in climatic conditions might cause

[1]Supported by the Deutsche Forschungsgemeinschaft (project KL 1806 5-1)

the GL to move substantially with considerable changes of the entire geometry of the ice sheet.

The physics of ice sheets becomes more complex when substantial parts are floating over the sea such that the effects of water must be accounted for. Indeed, ice sheets move mainly by ice deformation while floating ice shelves move mainly by basal sliding [39]. In between, some narrow transition zones where both processes play significant roles exhibit sharp changes in ice velocity profiles from shear-dominant to sliding-dominant. The motion of ice is usually described by a nonlinear Stokes equation, the ice being considered as an incompressible non-Newtonian fluid [19]. As a boundary condition, friction on the bedrock can be described by power-type, linear-type, or Coulomb laws [33] while perfect sliding occurs where ice is floating. In fact, only the vertical shear (resp. longitudinal) components of the stress tensor are significant in most of shallow ice sheets (resp. shelves) [39]. Simplified shallow ice models—that are mostly used by glaciologists—are derived from such observations. More precisely, simplifications occur by neglecting the terms where the small aspect ratio of ice sheets (in the order of 10^{-3}) appears in the dimensionless Stokes equations. As a result, the "Shallow Ice Approximation" (SIA) model [19] accounts only for the vertical shear. Similarly, the "Shallow Shelf Approximation" (SSA) model [33] accounts for the longitudinal stresses and the friction on the bedrock. In this paper, we implement an isothermal ice sheets and ice shelves model that is based on a superposition of the SIA model and of the SSA model [6, 39]. Such superposition assumes that the modelling of the horizontal and the vertical ice flows can be linearly decoupled. This assumption is physically justified for most ice sheets and ice shelves [39] and considerably reduces the size and the complexity of the system to solve.

In the last ten years, significant efforts were made to couple ice sheet and ice shelf models [7, 8, 13, 29, 34, 38, 39]. Among these contributions, one can distinguish two strategies for the numerical treatment of the GL. Since the grounded and floating domains evolve over time, one can follow the GL exactly or use an approximation. In both cases, the floating domain is determined by a geometrical criterion resulting from Archimedes principle. In the first case, we use this criterion to move the mesh together with the GL [7, 34]. Each domain (floating or grounded) involves a different model and a boundary condition imposes the continuity of stresses at the GL. Moving a one-dimensional mesh—that corresponds to a two-dimensional ice sheet—is an easy task since the GL is a single point. However, this becomes harder with one more horizontal dimension since the GL is a curve. For this reason, we adopt the second strategy in this paper. We use a unified model for the ice sheet and for the ice shelf with an implicit description of the GL through the flotation criterion. This criterion designs which points of the mesh are in the floating part and which points are in the grounded part such that different sliding conditions can be applied. We use a heuristic adaptive local mesh refinement procedure to deal with the sharp changes in the ice flow regime that are expected close to GL [9].

Existing shallow ice sheet and ice shelf models are often based on finite differences techniques [7, 29, 38, 39]. Such methods require structured meshes,

such that neither moving grids nor adaptive grid techniques can be straightforwardly combined. In contrast, finite element techniques—that are used in this paper—give a greater flexibility with respect to the mesh. Finite element techniques have been used to compute the ice flows in the context of marine ice sheets with a SSA model in [13] and a Stokes model in [8]. Following [24], we use a finite element scheme for the discretization and a nonlinear relaxation scheme combined with Newton-type multigrid corrections to solve the nonlinear problems. Such approach is comparable to the one implemented in [5] for a three-dimensional shallow model (called the first order approximation, see [4]). The special feature of our approach is, that nonsmoothness occurring in the SIA and SSA are more efficiently treated by truncation rather than by regularisation [15, 16].

In Section 2, we formulate the model for the time evolution of ice sheets and ice shelves that is based on the superposition "SIA + SSA" to describe isothermal ice flows. The model consists of two coupled variational inequalities: one deriving from a scalar p-Laplace (SIA) obstacle problem with a convection term and one deriving from a vectorial p-Laplace (SSA). In Section 3, we reformulate both p-Laplace problems as minimization problems and approximate them using the "Truncated Nonsmooth Newton MultiGrid" (TNMMG) method [15, 16]. A vertex-centred finite volume method is advocated to solve the convection part of the model. In Section 4, we apply our method to the test problems proposed by the Marine Ice Sheet Model Inter-comparison Project (MISMIP) in two- and three-dimensions [30, 31]. In particular, we discuss the effects of the adaptive mesh procedure on the reversibility of the GL under some perturbations in the ice flow and sliding parameters.

2. Model

In the following we describe two- and three-dimensional ice sheet models starting with the latter. For the three-dimensional model ($d = 3$), the ice sheet extends over a two-dimensional horizontal domain contained in $\Omega \subset \mathbb{R}^2$. Its height and all other quantities will be described as functions over Ω. If we assume that the three-dimensional ice sheet is constant in one horizontal direction y, we can describe it on a single vertical section at $y = 0$, leading to a two-dimensional ice sheet model ($d = 2$), see Fig. 1. In this model the ice sheet extends over a one-dimensional horizontal domain contained in $\Omega \subset \mathbb{R}$ that is orthogonal to the direction y of constant shape. Although such ice sheet is not physical, it is useful for the sake of understanding.

In any case we assume that $\Omega \subset \mathbb{R}^{d-1}$ is an open set (a segment if $d = 2$ or a rectangle if $d = 3$) that represents the horizontal support of the ice sheet. The d-dimensional volume of grounded or floating ice is then contained in $\Omega \times \mathbb{R}$ and described by functions over Ω. We denote the horizontal coordinates by $\mathbf{x} \in \Omega$ with $\mathbf{x} = (x, y)$ for $d = 3$ and $\mathbf{x} = x$ for $d = 2$ and the vertical coordinate by z.

In this paper $\nabla = \nabla_{\mathbf{x}}, \nabla\cdot = \nabla_{\mathbf{x}}\cdot$ denote gradient and divergence, respectively, in the horizontal variables $\mathbf{x}$. Let $[0, T]$ be a time interval, with $T > 0$. We suppose a fixed bedrock described by the elevation function $z = b(\mathbf{x})$ in Ω,

and we denote by $l = l(\mathbf{x}, t)$ and $s(\mathbf{x}, t)$ the elevation of the lower and upper ice surfaces at time t and abscissa $\mathbf{x}$, respectively. Obviously, the inequality $b(\mathbf{x}) \leq l(\mathbf{x}, t) \leq s(\mathbf{x}, t)$ holds for all $\mathbf{x} \in \Omega$ and all $t \in [0, T]$, $b = l$ where ice is grounded, $l > b$ where ice is floating and $l = s$ outside the ice domain Ω, see Fig. 1. We denote by $h = s - l$ the ice thickness function. In our model, s, l and h are continuous functions over Ω such that ice–water vertical cliffs are only allowed at the boundaries of Ω.

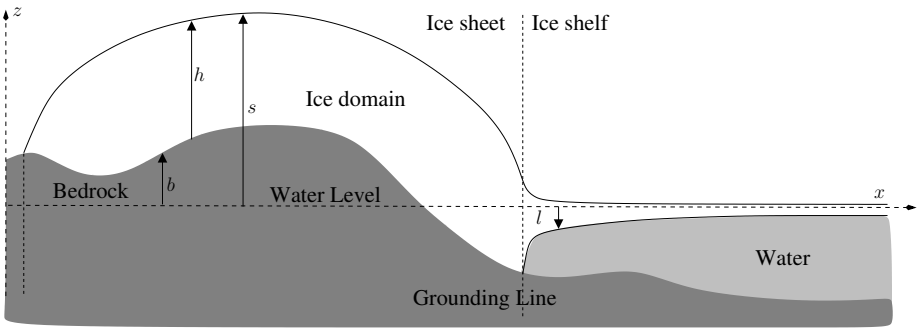

Figure 1: Vertical section of a system ice sheet/shelf with notations.

2.1. Shelf floatation

The floatation of ice is driven by Archimedes principle. Call g the acceleration of gravity, ρ and ρ_w the densities of ice and water, respectively. At any point $\mathbf{x}$ such that $h(\mathbf{x}) > 0$, if the buoyancy $-\rho_w g b(\mathbf{x})$ exceeds the force exerted by ice $\rho g h(\mathbf{x})$, then ice is floating, otherwise ice is grounded. Moreover, when ice is floating, the thickness of the rising part is $(1 - (\rho/\rho_w))$ of the total ice thickness. The application of Archimedes principle can be summarized by the relation

$$l = \max\left\{b, -\frac{\rho}{\rho_w} h\right\}. \tag{1}$$

The set of points $\mathbf{x}$ satisfying $b(\mathbf{x}) + \frac{\rho}{\rho_w} h(\mathbf{x}) = 0$ is the so-called "Grounding Line" (GL), which delimits the grounded and floating parts.

2.2. Velocity field

Following [6], the horizontal velocity field $\mathbf{u}_{TOT}(\mathbf{x}, z, t) \in \mathbb{R}^{d-1}$ of any ice particle in the ice domain $\{(\mathbf{x}, z) \in \Omega \times \mathbb{R},\ l(\mathbf{x}) \leq z \leq s(\mathbf{x})\}$ is the sum of a constant in z component $\mathbf{u}_{SSA}$ and a non constant component $\mathbf{u}_{SIA}$ [39]

$$\mathbf{u}_{TOT} = \mathbf{u}_{SIA} + \mathbf{u}_{SSA}. \tag{2}$$

Here, $\mathbf{u}_{SIA}(\mathbf{x}, z, t) \in \mathbb{R}^{d-1}$ is the horizontal velocity resulting from ice shearing which is described by the "Shallow Ice Approximation" (SIA), while $\mathbf{u}_{SSA}(\mathbf{x}, t) \in \mathbb{R}^{d-1}$ (also called $\mathbf{u}$) is the horizontal velocity induced by longitudinal stresses

which is described by the "Shallow Shelf Approximation" (SSA). The SIA and the SSA models are described in detail in Section 2.4 and 2.5, respectively. The vertical component of the velocity (never computed later) can be determined by using the incompressibility of ice. Where there is no ice ($h = 0$), $\mathbf{u}_{TOT}$, $\mathbf{u}_{SIA}$, and $\mathbf{u}_{SSA}$ are arbitrarily set to zero. To simplify the presentation, we assume in Sections 2 and 3 no ice inflows at the domain boundary $\partial\Omega$.

2.3. Mass conservation

The mass conservation principle in a vertical column of ice can be written as [19, 28]

$$\frac{\partial h}{\partial t} + \nabla \cdot \mathbf{q}_{TOT} = a, \tag{3}$$

where $a = a(\mathbf{x})$ is the yearly-averaged positive or negative external ice mass balance due to melting and solid precipitation, and

$$\mathbf{q}_{TOT} := \int_l^s \mathbf{u}_{TOT}(z)dz = \int_l^s \mathbf{u}_{SIA}(z)dz + h\mathbf{u}_{SSA} =: \mathbf{q}_{SIA} + \mathbf{q}_{SSA} \tag{4}$$

defines the total horizontal ice flux that can be split into $\mathbf{q}_{SIA}$ and $\mathbf{q}_{SSA}$ which derive from $\mathbf{u}_{SIA}$ and $\mathbf{u}_{SSA}$, respectively. Equation (3) says that the variation of ice thickness plus the divergence of the ice flux equals the external ice mass balance.

For simplicity, we assume that $a > 0$ where $b < 0$ such that there is always some ice over water. This assumption ensures that no ice–water cliff can appear outside the boundaries of the domain. By this assumption, we do not need to include a calving model for the erosion of the ice shelf margins.

2.4. Shallow Ice Approximation (SIA)

The isothermal SIA model describes the velocity profile $\mathbf{u}_{SIA}$ as a function of the ice thickness h, the vertical component z, the surface elevation s and its gradient ∇s [19, 28]:

$$\mathbf{u}_{SIA}(\mathbf{x}, z, t) = -(2A/p)(\rho g)^{p-1}\left[h^p - (s-z)^p\right]|\nabla s|^{p-2}\nabla s, \tag{5}$$

where $A > 0$ is the ice softness, p is a constant exponent linked to Glen's exponent $\bar{n}$ by the relation $p = \bar{n} + 1$ and $|\ |$ denotes the Euclidean norm. The most realistic value for $\bar{n}$ is found empirically close to 3 [28], consequently we assume $p > 2$. Using (4) and (5), the contribution of the SIA component to the horizontal ice flux is

$$\mathbf{q}_{SIA} = \int_l^s \mathbf{u}_{SIA}(z)dz = -\Gamma h^{p+1}|\nabla s|^{p-2}\nabla s, \tag{6}$$

where $\Gamma = 2A(\rho g)^{p-1}/(p+1) > 0$. Equations (3), (4), and (6) yield a single partial differential equation for the surface elevation h:

$$\frac{\partial h}{\partial t} - \Gamma\nabla \cdot \left(h^{p+1}|\nabla(h+l)|^{p-2}\nabla(h+l)\right) + \nabla \cdot (h\mathbf{u}_{SSA}) = a. \tag{7}$$

Note that $h \geq 0$ on Ω and equation (7) acts only over $\Omega_+ := \{\mathbf{x} \in \Omega, h(\mathbf{x}) > 0\}$. Clearly, $h(\mathbf{x}) = 0$ if $\mathbf{x} \in \Omega \cap \partial\Omega_+$ since h is continuous over Ω. Otherwise, we impose

$$\nabla s \cdot \mathbf{n} = 0, \quad \text{on } \partial\Omega \cap \partial\Omega_+, \tag{8}$$

such that, from (6), we have

$$\mathbf{q}_{SIA} \cdot \mathbf{n} = 0, \quad \text{on } \partial\Omega_+. \tag{9}$$

Moreover, one can easily show [23] that

$$\mathbf{q}_{SIA} = \mathbf{0}, \quad \text{and} \quad a \leq 0, \quad \text{on } \Omega \setminus \Omega_+. \tag{10}$$

Following [23], equation (7) takes the form of an obstacle problem which incorporates the free-boundary constraint through the condition $h \geq 0$. From (7), (9), (10) and Gauss theorem, the corresponding variational inequality writes [23]: for each $t \in [0, T]$, we find $h(t) \geq 0$ such that, for all $\varphi \geq 0$,

$$\int_\Omega \frac{\partial h}{\partial t}(\varphi - h)dV + \Gamma \int_\Omega h^{p+2}|\nabla h + \nabla l|^{p-2}(\nabla h + \nabla l) \cdot \nabla(\varphi - h)dV + \int_\Omega \nabla \cdot (h\,\mathbf{u}_{SSA})\,(\varphi - h)dV \geq \int_\Omega a(\varphi - h)dV. \tag{11}$$

Advantageously, the formulation (11) does not involve the unknown boundary of the ice domain $\{\mathbf{x} \in \Omega;\ h(\mathbf{x}) > 0\}$.

2.5. Shallow Shelf Approximation (SSA)

In the isothermal SSA model, the driving basal stress is partly balanced by the longitudinal stress (dominant at floating parts) and by the local stress at the base (dominant at grounding parts). More precisely, $\mathbf{u}_{SSA} = \mathbf{u}(\mathbf{x}, t)$ is determined by [33]

$$-A^{1-q}\,\nabla \cdot \Big(h\,|D(\mathbf{u})|_*^{q-2}\,[D(\mathbf{u}) + \mathrm{tr}(D(\mathbf{u}))I]\Big) + C|\mathbf{u}|^{m-1}\mathbf{u} \times \mathbf{1}_{G(h)} = -\rho g h \nabla s, \quad \text{if } |\mathbf{u}| > 0, \tag{12}$$

$$\mathbf{u} = 0, \quad \text{else}, \tag{13}$$

where $q = p/(p-1) \in (1, 2)$ is the conjugate exponent to p, $\mathbf{1}_{G(h)}$ is a bi-valued function equal to one in the grounded part

$$G(h) := \{\mathbf{x} \in \Omega, \quad b(\mathbf{x}) + (\rho/\rho_w)h(\mathbf{x}, \cdot) > 0, \quad h(\mathbf{x}, \cdot) > 0\}, \tag{14}$$

and to zero outside $G(h)$, $D(\mathbf{u}) := \frac{1}{2}\left(\nabla \mathbf{u} + \nabla \mathbf{u}^t\right)$ denotes the strain-rate of $\mathbf{u}$, tr is the trace operator, I the identity second order tensor and $|\cdot|_*$ denotes the norm $|X|_* := \sqrt{(X, X)_*}$ associated with the scalar product defined by

$$(X, Y)_* := \frac{1}{2}\left(\mathrm{tr}(XY) + \mathrm{tr}(X)\mathrm{tr}(Y)\right).$$

Here, $m \geq 0$ is a given parameter and $C = C(\mathbf{x}) > 0$ is a prescribed bed yield stress. The term $\mathbf{1}_{G(h)}$ in equation (12) vanishes outside $G(h)$ since no basal shear stress occurs under the ice shelf. Heuristically, the first term in (12) represents the longitudinal stresses, the second term represents the friction on the bedrock and the right-hand-side represents the gravitational driving force. The case $m = 0$ corresponds to the "plastic" Coulomb-type law in [35]. Note that if $A = 0$, $m > 0$, and without shelf, equation (12) can be rewritten as $\mathbf{u} = -\frac{1}{C}(\rho g h|\nabla s|)^{1/m}$ corresponding to Wertman's local sliding law [19]. Conditions on the boundary $\partial\Omega$ change if there is still ice on this boundary, if this ice is floating, grounded above or below sea level [33, 39]. However, such boundary conditions can be written in a unified way:

$$A^{1-q}\, h|D(\mathbf{u})|_*^{q-2}[D(\mathbf{u}) + \mathrm{tr}(D(\mathbf{u}))I] \cdot \mathbf{n} = \underbrace{\frac{1}{2}\rho g \left(h^2 - \frac{\rho_w}{\rho}[\min\{l, 0\}]^2 \right) \mathbf{n}}_{:=\mathbf{F}(h)}, \quad (15)$$

where l is defined by (1). Three cases might occur on the boundary $\partial\Omega$ in equation (15):

i) Ice is grounded above sea level, then $\mathbf{F}(h) = \frac{1}{2}\rho g h^2 \mathbf{n}$.

ii) Ice is grounded below sea level, then $\mathbf{F}(h) = \frac{1}{2}\rho g(h^2 - \frac{\rho_w}{\rho} b^2)\mathbf{n}$.

iii) Ice is floating, then $\mathbf{F}(h) = \frac{1}{2}\rho g h^2 (1 - \frac{\rho}{\rho_w})\mathbf{n}$.

Clearly, if there is no ice ($h = 0$), then $\mathbf{F}(h) = \mathbf{0}$. The case i) almost never appears in reality, since vertical ice cliffs are most of the time induced by the presence of water and calving processes. In the other cases, condition (15) says that the outward pressure of ice is partially balanced by the hydrostatic sea water pressure [33].

Equation (12) with boundary condition (15) can be reformulated as the variational inequality [33]

$$A^{1-q} \int_\Omega h|D(\mathbf{u})|_*^{q-2}(D(\mathbf{u}), D(\mathbf{v} - \mathbf{u}))_* dV + \frac{1}{m+1} \int_{G(h)} C(|\mathbf{v}|^{m+1} - |\mathbf{u}|^{m+1}) dV$$
$$+ \rho g \int_\Omega h \nabla s \cdot (\mathbf{v} - \mathbf{u}) dV - \int_{\partial\Omega} \mathbf{F}(h) \cdot (\mathbf{v} - \mathbf{u}) dS \geq 0, \quad (16)$$

where $\mathbf{v}$ is a test function. Like (11), the variational inequality (16) is attractive since it does not involve the boundary of the ice domain $\{\mathbf{x} \in \Omega;\ h(\mathbf{x}) > 0\}$. When $m > 0$, the inequality (16) can be actually rewritten as a variational equality [35].

2.6. Whole problem

For a given initial condition $h(\cdot, 0) = h_0(\cdot)$, our goal is to find $h(\cdot, t)$ and $\mathbf{u}(\cdot, t)$ that solve the system of equations (11) (16) for $t \in [0, T]$. The next section is dedicated to the approximation of solutions for this system.

3. Approximations

3.1. Time approximation

Let $N > 0$ be given, and $[t_0, ..., t_{N+1}]$ be a time discretization of $[0, T]$ with time steps $\tau_n = t_{n+1} - t_n, n = 0, 1, ..., N$. Let us denote by h_n, l_n, s_n, $\mathbf{u}_n$ some time approximations of $h(t_n)$, $l(t_n)$, $s(t_n)$ and $\mathbf{u}(t_n)$ for all $n = 0, 1, ..., N + 1$.

First we note that the variational inequality (16) for the SSA part can be rewritten as a minimization problem [33] (step I below). The variational inequality (11) for the SIA part is derived from a nonlinear diffusion–advection equation (7) that is expected to be advection-dominated on the floating part and diffusion-dominated on the grounded part. Operator splitting techniques [12, chapter 2] for solving (11) are used to decouple the advection operator from the diffusion operator. A first order operator splitting corresponds to solving the equation, first without diffusion with appropriate initial conditions and second without the advection term and source terms. Using this operator splitting for a semi-implicit discretisation of (11) leads to a transport problem (step II below) and a variational inequality that can also be written as a minimization problem [23] (step III below). Finally, assuming h_n known for some n, the three steps below describe how to compute h_{n+1}.

Step I: Find $\mathbf{u}_n$ that minimizes

$$\mathcal{J}_{SSA}(\mathbf{v}) := \frac{2A^{1-q}}{q} \int_\Omega h_n |D(\mathbf{v})|_*^q dV + \frac{1}{m+1} \int_{G(h_n)} C|\mathbf{v}|^{m+1} dV + \rho g \int_\Omega h_n \nabla s_n \cdot \mathbf{v} dV - \int_{\partial\Omega} \mathbf{F}(h_n) \cdot \mathbf{v} dS, \tag{17}$$

where $s_n = l_n + h_n$, and l_n is computed from (1) with h_n.

Step II: Find $h_{n+\frac{1}{2}}$, the solution at time t_{n+1} of the advection problem

$$\begin{cases} \dfrac{\partial h}{\partial t} + \nabla \cdot (h\mathbf{u}_n) = 0, & \text{on} \quad (t_n, t_{n+1}), \\ h(t_n) = h_n. \end{cases} \tag{18}$$

Step III: Find $h_{n+1} \geq 0$ that minimizes over all $\varphi \geq 0$

$$\mathcal{J}_{SIA}(\varphi) := \frac{1}{2\tau_n} \int_\Omega \varphi^2 dV + \frac{\Gamma}{p} \int_\Omega (h_{n+\frac{1}{2}})^{p+2} \left| \nabla\varphi + \nabla l_{n+\frac{1}{2}} \right|^p dV - \int_\Omega \left(\frac{h_{n+\frac{1}{2}}}{\tau_n} + a \right) \varphi dV, \tag{19}$$

where $l_{n+\frac{1}{2}}$ is computed from (1).

If one does not need to account for the SIA velocity in our model (i.e. $\mathbf{u}_{TOT} = \mathbf{u}_{SSA}$ in (2)), step III is simply replaced by

$$h_{n+1} = \max(h_{n+\frac{1}{2}} + a\tau_n, 0).$$

If $G(h_n)$ has a positive measure, one can show that the functional $\mathcal{J}_{SSA}$ is strictly convex, strongly continuous in $W^{1,q}(\Omega)^{d-1}$ and therefore lower semicontinuous [33, 35]. However, coerciveness would require h_n to be uniformly lower bounded by a positive constant and $m > 0$. The case $m = 0$, namely Coulomb friction or "plastic till", requires further hypothesis [35]. As a consequence the well-posedness of the minimization problem related to $\mathcal{J}_{SSA}$ is not guaranteed since h_n might tend to zero. In the same way, one can show that $\mathcal{J}_{SIA}$ is strictly convex, strongly continuous in $\{v \in W^{1,p}(\Omega), v \geq 0\}$ and then lower semicontinuous [23]. However, since $h_{n+\frac{1}{2}}$ is not uniformly lower bounded, coerciveness and then well-posedness of the minimization problem are not guaranteed.

3.2. Space approximation

The minimization problems of steps I and III both derive from a nonlinear p-Laplace problem, however, with $p < 2$ in step I and $p > 2$ in step III. Finite element approximations of p-Laplace problems were proposed and analysed in [2]. More specifically, the obstacle problem resulting from the mass conservation and the SIA in a steady state shape (similar to the one of step III) was treated in [23]. Likewise, the problem of step I was analysed in [35]. Multigrid algorithms for the p-Laplace problem have been proposed and analysed in [3, 21]. There are two basic approaches to implement multigrid methods for convex nonlinear minimization problems [26]. The first approach consists of linearizing the problem and using a multigrid solver for the remaining linear problems. This strategy was adopted in [21], where multigrid was used to solve the linearized subproblems in a damped Newton-like descent method. The second approach applies the multigrid methodology directly in the original nonlinear equation with a nonlinear smoother. As an example, the full approximation scheme with a Polak–Ribiere conjugate gradient method as smoother was applied in [3]. An obstacle constraint induces an additional nonsmooth nonlinearity that cannot be directly tackled by a Newton-type method that requires smoothness. To account for nonsmooth nonlinearities, we might use some additional methods such as primal–dual active set or truncated monotone multigrid [15, 25]. In Section 3.2.1, we adopt a closely relative approach, more precisely, the Truncated Nonsmooth Newton MultiGrid (TNNMG) method [14, 15, 16].

A number of schemes exist to solve the transport problem (18) (step II) including finite differences [6, 39], finite elements [9] or finite volumes [10]. We opt for the latter and discuss the details in Section 3.2.2.

Assume $\mathcal{T}_\mathtt{h}$ to be a mesh of $\Omega \subset \mathbb{R}^{d-1}$, which exactly covers Ω, that is made of segments when $d = 2$ and of triangles when $d = 3$. The mesh $\mathcal{T}_\mathtt{h}$ is parametrized by $\mathtt{h}$, the size of its highest diameter element, and satisfies three fundamental assumptions. First, we assume that $\mathcal{T}_\mathtt{h}$ is *regular* in the sense that it consists of a finite number of non-degenerate simplices. Second, we assume the mesh to be *conforming* [11], i.e. the intersection of any pair of element boundaries is either empty or an entire boundary of the two elements. Third, we suppose $\mathcal{T}_\mathtt{h}$ to be *hierarchic* (or multilevel), i.e. $\mathcal{T}_\mathtt{h}$ results from several levels of local or global refinement applied to an initial coarse mesh of Ω. Such hierarchy is necessary

to apply the geometric multigrid method in Section 3.2.1. Since we implement in Section 3.2.3 an adaptive mesh refinement procedure, the mesh $\mathcal{T}_\mathtt{h}$ changes with the time step n, i.e. $\mathcal{T}_\mathtt{h} = \mathcal{T}_{\mathtt{h},n}$. For simplicity, we omit the dependence on n until Section 3.2.3.

We now introduce some notations related to $\mathcal{T}_\mathtt{h}$ that will be used in Sections 3.2.1 and 3.2.2. The mesh $\mathcal{T}_\mathtt{h}$ contains I nodes $\{\mathbf{p}_i\}_{i=1,..,I} \subset \mathbb{R}^{d-1}$ and L elements $\{e_l\}_{l=1,...,L}$. We will later consider the finite element space $\mathcal{V}_\mathtt{h}$ spanned by the continuous, linear on each element of $\mathcal{T}_\mathtt{h}$ functions λ_i, defined by $\lambda_i(\mathbf{p}_j)$ equals one if $i = j$ and zero else. We call $h_{\mathtt{h},n}$, $l_{\mathtt{h},n}$, $s_{\mathtt{h},n} \in \mathcal{V}_\mathtt{h}$ and $\mathbf{u}_{\mathtt{h},n} \in \mathcal{V}_\mathtt{h}^{d-1}$ some approximations in space of h_n, l_n, s_n and $\mathbf{u}_n$. The approximation $h_{\mathtt{h},n}$ can be identified with the set of nodal values $\{H_i, i = 1, .., I\}$ for the finite element space $\mathcal{V}_\mathtt{h}$ since (dropping n) $h_\mathtt{h} = \sum_{1,..,I} H_i\lambda_i$. The same identification holds for $l_{\mathtt{h},n}$, $s_{\mathtt{h},n}$ and $\mathbf{u}_{\mathtt{h},n}$.

3.2.1. Minimization problems (steps I and III)

The Ritz–Galerkin approximation of the first minimization problem (step I) in this finite element space $[\mathcal{V}_\mathtt{h}]^{d-1}$ can be written directly in the following form:

$$\text{Find } \mathbf{U} = \{\mathbf{U}_i\}_{i=1,...,I} \in [\mathbb{R}^I]^{d-1} \quad \text{s.t.} \quad \mathcal{J}^\mathtt{h}_{SSA}(\mathbf{U}) \le \mathcal{J}^\mathtt{h}_{SSA}(\mathbf{V}), \quad \forall \mathbf{V} \in [\mathbb{R}^I]^{d-1},$$

where

$$\mathcal{J}^\mathtt{h}_{SSA}(\mathbf{V}) := \sum_{l=1}^{L} \alpha_l \left| \sum_{j\in e_l} \mathbf{V}_j D_{|e_l}(\lambda_j) \right|_*^q + \sum_{i=1}^{I} \beta_i |\mathbf{V}_i|^{m+1} + \sum_{i=1}^{I} \mathbf{G}_i \cdot \mathbf{V}_i - \sum_{i=1}^{I} \mathbf{F}_i \cdot \mathbf{V}_i, \tag{20}$$

and

$$\alpha_l := \frac{2A^{1-q}}{q} \int_{e_l} h_{\mathtt{h},n} dV, \qquad \beta_i := \frac{1}{m+1} \int_{G(h_n)} C\lambda_i dV,$$
$$\mathbf{G}_i := \rho g \int_\Omega h_{\mathtt{h},n} \nabla s_{\mathtt{h},n} \lambda_i dV, \qquad \mathbf{F}_i := \int_{\partial\Omega} \mathbf{F}(h_{\mathtt{h},n})\lambda_i dS. \tag{21}$$

In the same way, the Ritz–Galerkin approximation of the second minimization problem (step III) in the same finite element space $\mathcal{V}_\mathtt{h}$ writes:

$$\text{Find } H = \{H_i\}_{i=1,...,I} \in \mathbb{R}^I \quad \text{s.t.} \quad \mathcal{J}^\mathtt{h}_{SIA}(H) \le \mathcal{J}^\mathtt{h}_{SIA}(\Phi), \quad \forall \Phi \in \mathbb{R}^I,$$

where

$$\mathcal{J}^\mathtt{h}_{SIA}(\Phi) = \sum_{i=1}^{I} \gamma_i \Phi_i^2 + \sum_{l=1}^{L} \mu_l \left| \sum_{j\in e_l} (\Phi_j + l_{n+\frac{1}{2},j}) \nabla_{|e_l} \lambda_j \right|^p - \sum_{i=1}^{I} f_i \Phi_i + \sum_{i=1}^{I} \chi(\Phi_i), \tag{22}$$

and

$$\gamma_i := \frac{1}{2\tau_n}\int_\Omega \lambda_i dV, \quad \mu_l := \frac{\Gamma}{p}\int_{e_l} (h_{\mathtt{h},n+\frac{1}{2}})^{p+2} dV, \quad f_i := \int_\Omega \left(\frac{h_{\mathtt{h},n+\frac{1}{2}}}{\tau_n} + a\right)\lambda_i dV, \tag{23}$$

where χ is the function defined by $\chi(a) = \begin{cases} 0, & \text{if } a \geq 0, \\ +\infty, & \text{else.} \end{cases}$

Since $h_{\mathtt{h},n+\frac{1}{2}}$ and $s_{\mathtt{h},n+\frac{1}{2}}$ are linear on each element, the integrals in (21) (23) can be computed exactly by using numerical quadratures with a sufficiently large order. This is also true for β_i if C is constant. However, in practice, this is not needed, such that $\mathcal{J}_{SSA} \neq \mathcal{J}^{\mathtt{h}}_{SSA}$ and $\mathcal{J}_{SIA} \neq \mathcal{J}^{\mathtt{h}}_{SIA}$.

Eventually, the Ritz–Galerkin approximation of the two minimization problems (steps I and III) in the standard continuous linear finite element space can be written in a unified form:

$$\text{Find} \quad U \in \mathbb{R}^J \quad \text{s.t.} \qquad \mathcal{J}(U) \leq \mathcal{J}(V), \qquad \forall V \in \mathbb{R}^J, \tag{24}$$

where $J \in \mathbb{N}$, $\mathcal{J} : \mathbb{R}^J \longrightarrow \mathbb{R} \cup \{+\infty\}$ is strictly convex, coercive, lower semi-continuous, but not necessary smooth. Indeed, the case $m = 0$ in (20) or the function χ in (22) (generated by the obstacle) are two nonsmooth terms in $\mathcal{J}^{\mathtt{h}}_{SSA}$ and $\mathcal{J}^{\mathtt{h}}_{SIA}$, respectively. Also, $\mathcal{J}^{\mathtt{h}}_{SIA}$ and $\mathcal{J}^{\mathtt{h}}_{SSA}$ are coercive in the finite dimensional space since all norms are equivalent.

Following the techniques that have been developed in [14, 15, 16] for linear and nonlinear problems with obstacle, we now describe the TNNMG method for minimization problems of type (24). The key assumption of the TNNMG method as presented here is, that the nonsmooth part of the energy functional $\mathcal{J}$ is separable, i.e. it decomposes with respect to the one-dimensional Euclidean directions. The latter is true for $\mathcal{J}^{\mathtt{h}}_{SIA}$ and, if $d = 2$, also for $\mathcal{J}^{\mathtt{h}}_{SSA}$.

Define the nonlinear Gauß–Seidel smoother $\mathcal{F} : \mathbb{R}^J \to \mathbb{R}^J$ by

$$\mathcal{F}(U)_i = \text{argmin}_{\rho \in \mathbb{R}} \mathcal{J}\left(U + \sum_{j=1}^{i-1} \mathcal{F}(U)_j E_j + \rho E_i\right), \qquad \forall i = 1, ..., J, \tag{25}$$

where $\{E_i, i = 1, ..., J\}$ denotes the canonical base of $\mathbb{R}^J$. One Gauß–Seidel iteration consists of minimizing successively $\mathcal{J}$ in all coordinate directions. Here, the nonlinear scalar minimization problems (25) are solved inexactly by using a bisection method which does not require any smoothness on $\mathcal{J}$.

For $d = 3$ the nonsmooth part in $\mathcal{J}^{\mathtt{h}}_{SSA}$ does only decouple into local two-dimensional problems because of the Euclidean norm $|\cdot|$ in (20). In this case the TNNMG method as introduced below will in general only converge if the Gauß–Seidel method is replaced by a block Gauß–Seidel method solving local two-dimensional problems. For simplicity we omit the details and restrict ourselves to $d = 2$ if $m = 0$ in the following.

The TNNMG method defines a sequence $\{U^\nu\}$ by

$$U^{\nu+\frac{1}{2}} = U^\nu + \mathcal{F}(U^\nu), \tag{26}$$

$$\mathcal{I}^\nu = \mathcal{I}(U^{\nu+\frac{1}{2}}) \tag{27}$$

$$V^{\nu+\frac{1}{2}} = -(\mathcal{J}''(U^{\nu+\frac{1}{2}})_{\mathcal{I}^\nu,\mathcal{I}^\nu})^+ \mathcal{J}'(U^{\nu+\frac{1}{2}})_{\mathcal{I}^\nu}, \tag{28}$$

$$V^{\nu+1} = \mathcal{P}_{\mathrm{Dom}(\mathcal{J})-U^{\nu+\frac{1}{2}}}(V^{\nu+\frac{1}{2}}), \tag{29}$$

$$U^{\nu+1} = U^{\nu+\frac{1}{2}} + \rho^\nu V^{\nu+1}, \tag{30}$$

where

$$\rho^\nu = \mathrm{argmin}_{\rho\in[0,\infty)} \mathcal{J}(U^{\nu+\frac{1}{2}} + \rho V^{\nu+1}), \tag{31}$$

$$\mathcal{I}(V) = \{i \ : \ \text{the subdifferential } \partial\mathcal{J}(V_i) \ \text{ is single-valued } \}, \tag{32}$$

and where $N_\mathcal{I}$ and $\mathcal{M}_{\mathcal{I},\mathcal{I}}$ are the vectors and matrices truncated to the set of indices $\mathcal{I}$ for any vector N and any matrix M, i.e. the elements of the i-th line (and i-th column of the matrix) that are not in $\mathcal{I}$ are set to zero. Here, $\mathcal{P}_{\mathrm{Dom}(\mathcal{J})-U}$ denotes the projection on the convex set $\mathrm{Dom}(\mathcal{J}) - U = \{V \ : \ \mathcal{J}(U+V) < +\infty\}$.

Step (26) consists of one smoother iteration that successively minimizes the energy functional in the scalar coordinate directions. Then the inactive set $\mathcal{I}^\nu$ is selected (27), such that $\mathcal{J}$ is (locally) smooth on the subspace

$$\mathbb{R}^I_{\mathcal{I}^\nu} := \{V \in \mathbb{R}^I, V_i = 0 \text{ if } i \notin \mathcal{I}^\nu\} \tag{33}$$

spanned by the inactive components. The $(\cdot)^+$ in step (28) denotes the Moore–Penrose pseudoinverse [36] which is effectively the inverse on the subspace $\mathbb{R}^I_{\mathcal{I}^\nu}$, such that (28) is a Newton correction on this subspace. Note that, due to the selection of $\mathcal{I}^\nu$, all necessary derivatives of $\mathcal{J}$ exist on this subspace. Since the application $U^{\nu+\frac{1}{2}} + V^{\nu+\frac{1}{2}}$ of the Newton correction might lead outside the convex set $\mathrm{Dom}(\mathcal{J})$, the projection step (29) is advocated to constrain the new iterate to remain in $\mathrm{Dom}(\mathcal{J})$. Since the projected correction does not necessarily decrease the energy, a damping parameter in step (30) ensures the monotonicity of the scheme and the global convergence of the method [15]. It remains to describe how to invert $\mathcal{J}''(U^{\nu+\frac{1}{2}})_{\mathcal{I}^\nu,\mathcal{I}^\nu}$ in step (28). Multigrid methods are known to be one of the fastest approaches to solve linear systems resulting from discretized partial differential equations [20, 40]. A remarkable feature of multigrid methods are mesh-independent convergence rates. Since the matrix $\mathcal{J}''(U^{\nu+\frac{1}{2}})_{\mathcal{I}^\nu,\mathcal{I}^\nu}$ is symmetric and positive definite on the subspace $\mathbb{R}^I_{\mathcal{I}^\nu}$ we can apply a linear geometric multigrid method for the inversion of $\mathcal{J}''(U^{\nu+\frac{1}{2}})_{\mathcal{I}^\nu,\mathcal{I}^\nu}$ in the correction step (28).

The hierarchical (or multilevel) aspect of the mesh $\mathcal{T}_\mathtt{h}$ is crucial for the application of a geometric multigrid method. Indeed, such method relies on sequentially nested grids and the application of simple relaxation methods at all levels of the grid hierarchy. While a smoother on a fine grid is efficient to reduce the high frequencies of the error, the low frequencies are more efficiently

damped on coarser grids [40]. The multigrid method consists of the application of a smoother on all finite element spaces induced by the grids of the hierarchy in order to damp all frequencies of the error. As a special feature the matrix $\mathcal{J}''(U^{\nu+\frac{1}{2}})_{\mathcal{I}^\nu,\mathcal{I}^\nu}$ is in general only positive semi-definite on the whole space $\mathbb{R}^I$. The fact that the matrix is not invertible in general does not pose a problem since a standard linear multigrid method will automatically act on the space $\mathbb{R}^I_{\mathcal{I}^\nu}$ and implicitly use subspaces of $\mathbb{R}^I_{\mathcal{I}^\nu}$ for the coarse grid corrections [14].

We opt for a V-cycle type multigrid solver combined with a linear Gauß–Seidel smoother with 3 pre- and post-smoothing steps [20]. Since there is no need to solve the system (28) to a certain accuracy applying one single multigrid iteration is enough to reach global convergence. The implementation is based on the code *DUNE* (http://www.dune-project.org/dune.html) and the modules *Dune-Solvers* and *Dune-Tnnmg* [16].

The convergence of the TNNMG method for strongly convex energy functionals was proven in [14] for the Gauß–Seidel smoother defined by (25) and a variant with inexact solution of the scalar subproblems in (25). A generalization of the proof for strictly convex functionals is given in [18]. The convergence result remains true when replacing the nonlinear Gauß–Seidel smoother by the simpler Jacobi smoother, however, a damping must be advocated in step (26) to insure the global convergence.

3.2.2. Transport problem (step II)

In this section, we briefly describe how to solve (18) using a finite volume method [27]. The exact mass conservation is an attractive feature of this method. Since h_n takes nodal values, we opt for vertex-centered finite volumes. In one space dimension ($d = 2$), the finite volume at a given node is simply delimited by the midpoints of neighboring cells. In two space dimensions ($d = 3$), finite volumes are built by following the medians of all triangles, see Fig. 2. As an alternative, one could follow a strategy using Voronoi cell structures like in [10].

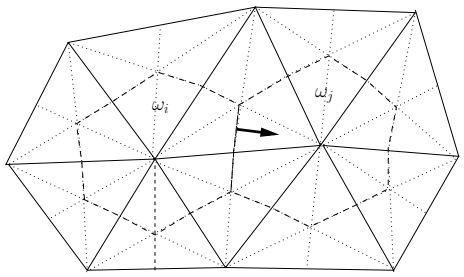

Figure 2: Illustration of vertex-centred finite volumes when $d = 3$. A few elements of the mesh $\mathcal{T}_\mathrm{h}$ are represented with continuous bold lines, the medians of all triangles are drawn with dotted lines and two finite volumes ω_i and ω_j are represented with dashed lines.

If we call ω_i the finite volume that is centred at node i, the value of h_n on

ω_i used for the transport scheme is identified to its nodal value $h_n(\mathbf{p}_i)$ defined in Section 3.2. With this identification, h_n does not need to be interpolated. We opt for a full upwind evaluation of the fluxes and an explicit Euler scheme in time. When $d = 2$, this scheme is strictly equivalent to the classical explicit upwind finite difference scheme, like the one used in [39]. For stability reason, this scheme cannot be performed with too large time step τ_n. The time step is then computed adaptively such that the CFL condition is fulfilled.

3.2.3. Fixed and adaptive grid strategies

Ice sheets exhibit strong variations of velocities between slow grounded parts and fast floating parts, i.e. in the neighbourhood of the Grounding Line (GL). Therefore, using a fixed mesh, it might be very expensive to capture such sharp changes in the dynamical regime of ice [31] with a reasonable accuracy. Thus an adaptive mesh refinement procedure is implemented to obtain a high accuracy close to the GL while keeping the computational effort moderate. The finite element and finite volume techniques detailed in Sections 3.2.1 and 3.2.2 are combined with a heuristic local mesh refinement procedure similar to the one used in [9]. Implementing an adaptive mesh occurs to build a new mesh $\mathcal{T}_\mathtt{h}$ of Ω at each time step n before starting step I, i.e. $\mathcal{T}_\mathtt{h} = \mathcal{T}_{\mathtt{h},n}$. We describe now how to build each mesh $\mathcal{T}_{\mathtt{h},n}$.

First, let us consider a regular, conforming and hierarchic mesh $\mathcal{T}^{\text{ref}}_{\mathtt{h}_{\max}}$ of the domain Ω, independent of n. If $d = 2$ (resp. $d = 3$), Ω is an interval (resp. a rectangle) and $\mathcal{T}^{\text{ref}}_{\mathtt{h}_{\max}}$ is simply obtained from j successive uniform refinements applied to an initial mesh $\mathcal{T}^0$ of Ω. If $d = 2$, the initial mesh $\mathcal{T}^0$ simply consists of the segment Ω. If $d = 3$, the initial triangulation $\mathcal{T}^0$ is built by splitting the rectangle Ω into one row of squares (or if this is not possible, into one row of rectangles with an aspect ratio close to one), each one being split into two congruent triangles, see Fig. 3. The mesh size of $\mathcal{T}^{\text{ref}}_{\mathtt{h}_{\max}}$ is then $\mathtt{h}_{\max} = |\Omega|/2^j$, where $|\Omega|$ is the smallest edge length of the rectangle Ω when $d = 3$. The mesh size $\mathtt{h}_{\max}$ should be sufficiently small to capture the solution far from the GL, i.e. where no sharp changes in the ice dynamics are expected.

Second, we build the mesh $\mathcal{T}_{\mathtt{h},n}$ at each time step n by locally refining $\mathcal{T}^{\text{ref}}_{\mathtt{h}_{\max}}$ where needed, i.e. close to GL_n. Here, GL_n denotes the GL at time t_n defined by

$$GL_n := \{\mathbf{x} \in \Omega, \quad b(\mathbf{x}) + (\rho/\rho_w)h_n(\mathbf{x}, \cdot) = 0, \quad h_n(\mathbf{x}, \cdot) > 0\}.$$

More precisely, we define an interval for a two-dimensional ice sheet and a band for a three-dimensional ice sheet around the GL

$$R = \{\mathbf{x}; \quad \text{dist}(\mathbf{x}, GL_n) < L_f\}, \tag{34}$$

where $L_f > 0$. Now all elements that intersect the band R are uniformly refined by dividing each interval (resp. triangle) into two adjacent subintervals (resp. four congruent subtriangles) when $d = 2$ (resp. $d = 3$), see Fig. 3. We repeat the procedure at several levels until the size of the smallest element reaches the value $\mathtt{h}_{\min}$ which represents the size of the mesh required close to

the GL. Finally a conforming mesh is constructed by adding some new nodes (black points on Fig. 3) between unrefined and refined regions. This procedure guarantees the conformity, the hierarchy, and the regularity of the mesh $\mathcal{T}_{\mathtt{h},n}$. Indeed, since lower and upper bounds of the interior angles are preserved in course of refinement, the elements cannot degenerate.

In addition to modify the mesh $\mathcal{T}_{\mathtt{h}}$, the quantity h_{n-1} needs to migrate from the mesh $\mathcal{T}_{\mathtt{h},n-1}$ to the new one $\mathcal{T}_{\mathtt{h},n}$. This is done by computing the linear interpolation of h_{n-1} at the nodes in $\mathcal{T}_{\mathtt{h},n}$. In regions where the mesh was coarsened compared to $\mathcal{T}_{\mathtt{h},n-1}$, the function h_{n-1} can in general not be represented exactly on $\mathcal{T}_{\mathtt{h},n}$, resulting in quadrature errors in the integrals in (21) (23). The latter can be avoided if both meshes, $\mathcal{T}_{\mathtt{h},n-1}$ and $\mathcal{T}_{\mathtt{h},n}$, are contained in a single, finer mesh hierarchy which will however introduce hanging nodes [17].

In Section 4, we refer to Fixed Grid (FG) strategy when using the mesh of reference directly without adaptation $\mathcal{T}_{\mathtt{h}} = \mathcal{T}^{\mathrm{ref}}_{\mathtt{h}_{\max}}$ and to Adaptive Grid (FG) strategy when using the locally refined mesh $\mathcal{T}_{\mathtt{h}} = \mathcal{T}_{\mathtt{h},n}$.

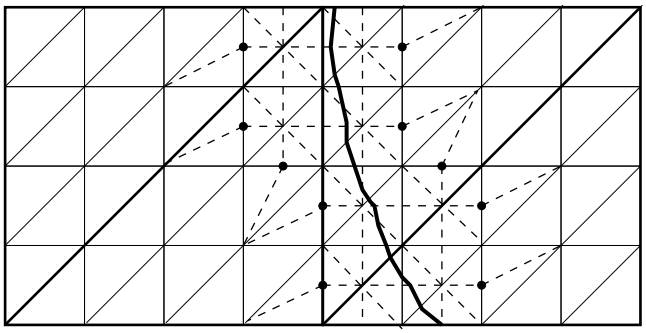

Figure 3: Illustration of the mesh refinement procedure when $d = 3$. The continuous bold lines represent the initial mesh $\mathcal{T}^0$, the continuous lines represent the reference mesh $\mathcal{T}^{\mathrm{ref}}_{\mathtt{h}_{\max}}$ and the dashed lines represent the additional mesh refinements. The union of continuous and dashed lines shape the final mesh $\mathcal{T}_{\mathtt{h},n}$, which is locally refined for the GL (bold line). Additional black points are required for the conformity of $\mathcal{T}_{\mathtt{h},n}$.

4. Results

In this section, we perform several simulations of idealized two- and three-dimensional ice sheets. First, a two-dimensional ice sheet with an attached shelf part is simulated until reaching a steady state shape. We analyse the behaviour of the SIA and SSA velocities and of the Grounding Line (GL) according to sliding and ice softness parameters. Second, we follow the test problems proposed in the Marine Ice Sheet Model Intercomparison Project (MISMIP) 2D [31] and we validate our results against an analytic solution. Eventually, we show some results related to the three-dimensional version of MISMIP, called MISMIP 3D

[30]. In the paper, the following physical parameters are used: $\rho = 900$ kg m^{-3}, $\rho_w = 1000$ kg m^{-3}, $\bar{n} = 3$ (or $p = 4$), and $g = 9.81$ m s^{-2}.

4.1. Influence of sliding and ice softness parameters

Let us consider the one-dimensional domain $\Omega = [-1000, 1000]$ km with the analytic curved bedrock as depicted in Fig. 4. We assume a bi-valued constant-in-time mass balance defined by $a(x) = -1$ m y^{-1} if $x < -500$ km and $a = 0.3$ m y^{-1} elsewhere. On the left-hand-side of the domain Ω, the ablation area allows a free grounded margin to shape on the bedrock which is above sea level. On the right-hand-side, the bedrock is below sea level and the mass balance is positive such that a shelf is generated up to the boundary of Ω. Four experiments are performed with different sets of parameters, see Table 1. As sliding law in equation (12), experiments a) and d) involve a power-type law, experiment b) involves a linear-type law and experiment c) involves a Coulomb-type law like in [33, 35]. Experiment d) corresponds to a), however, with a much smaller parameter A (corresponding to a more viscous ice). For each experiment, we initialize the ice geometry by a ten-meter-thick layer of ice (grounded and floating) on Ω and run the model until reaching a steady state shape. For the discretization we adopt a fixed grid strategy, i.e. the domain Ω is uniformly refined $\mathcal{T}_\mathtt{h} = \mathcal{T}_\mathtt{h}^{\text{ref}}$, but with a fine resolution: $\mathtt{h} = 1.7$ km.

Experiment	a	b	c	d
m	1/3	1	0	1/3
C	7.624×10^6	7.208×10^{10}	1.0×10^5	7.624×10^6
A	4.6416×10^{-24}			4.6416×10^{-26}

Table 1: Parameters for experiment a, b, c, and d. The units of C and A are Pa m^{-m} s^m and Pa^{-3} s^{-1}, respectively.

Ice sheets are considered to be steady when the normalized annual volume change is lower than 10^{-6}. Steady state shapes for experiments a), b), c), and d) were found after ~ 11, ~ 18, ~ 18 and ~ 20 millenniums, respectively. Fig. 4 displays the corresponding shapes with SIA and SSA velocity components. In contrast to the SSA velocities that were found by solving equation (16), the SIA velocity was obtained *a posteriori* from formula (5). Indeed, due to the inclusion of (5) in (3), there is no need to compute explicitly SIA velocities.

As expected, SSA velocities are dominant in the ice shelf. In contrast, SIA velocities play a significant role on the grounded part only when the gradient of the top surface elevation is sufficiently large and when A is not too small (formula (5)). Power or linear parametrizations of the sliding do not show major differences in ice velocities. However, the highest part of the steady ice sheet is smooth with the linear law while there is a visible jump in the derivatives with the power law corresponding to the well-known Raymond bump [32]. In contrast to power or linear laws, the Coulomb-type law displays SSA velocities only in the transition and floating areas. As expected, there is clear separation between

zero SSA velocity and non zero SSA velocity. Also, linear and power sliding laws induce steeper gradients of the top surface elevation at the Grounding Line (GL) position. In particular, this is visible at the GL, since both laws exhibit SIA velocities that tend to infinity (or, equivalently, the gradient of the top surface tends to infinity, see equation (5)). In contrast, Coulomb sliding law exhibits regular SIA velocities. As expected, taking a smaller A reduces both SSA and SIA velocities such that the ice sheet gets thicker and the GL stabilizes farer from the origin. This can also be observed when comparing the experiments a) and d) on Fig. 4. Simulating the effects of several values of A on the GL is the goal of the next section.

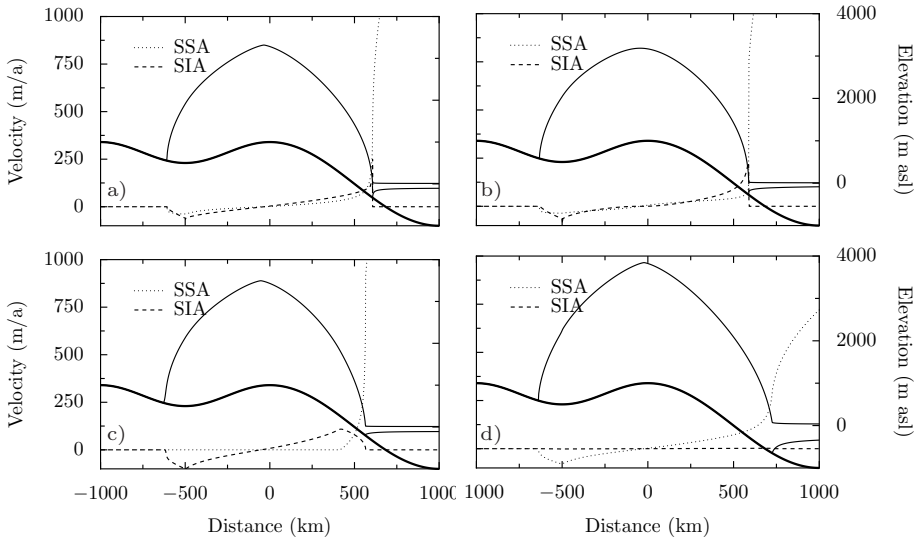

Figure 4: Steady state shapes for the various parametrizations of experiments a, b, c and d, see Table 1.

4.2. MISMIP 2D

The Marine Ice Sheet Model Intercomparison Project MISMIP (2D) consists of several simulation runs of a two-dimensional ice sheet and ice shelf that have been designed to allow a better comparison between marine ice sheet models [31]. In particular, the project aims to test the reversibility of the modelled Grounding Line (GL), i.e. its ability to recover its location after a perturbation in flow law parameters. This reversibility is physical on a downward-sloping bedrock. However, it is known that no GL can stabilize—and then be reversible—on upward-sloping bedrock [34]. Indeed, the ice discharge through the GL increases with the ice thickness [34]. As a consequence, any slight retreat of the GL on an upward-sloping bed would increase the ice thickness at the GL, increase the flux, and enhance the retreat. By such positive feedback effect, a marine ice sheet

might retreat in an irreversible way if a depression occurs on the bedrock. Such phenomenon—called hysteresis—is also a part of the MISMIP experiments.

We consider the one-dimensional domain $\Omega = [0, 2000]$ km. There are four experiments in MISMIP that differ by the choice of the bedrock, parameters C and m and by a set of parameters A, see Table 2. We use the labels 1a/2a, 1b/2b, 3a, and 3b, as originally introduced in [31]. On the one hand, experiments 1a/2a and 1b/2b use a bedrock with a constant slope while experiments 3a and 3b use a polynomial bedrock. They are respectively defined by

$$b(x) = 720 - 778.5\,(x/\bar{L}), \tag{35}$$

$$b(x) = 729 - 2184.8\,(x/\bar{L})^2 + 1031.72\,(x/\bar{L})^4 - 151.72\,(x/\bar{L})^6, \tag{36}$$

where $\bar{L} = 750$ km. On the other hand, experiments 1a/2a and 3a use a power-type sliding parametrization while experiments 1b/2b and 3b use a linear-type sliding parametrization. The accumulation rate is taken as constant, $a = 0.3$ m a^{-1}, for all experiments. Note that, symmetry is imposed at $x = 0$ km.

Experiment	1a/2a	1b/2b	3a	3b
Bedrock	sloppy-flat bed, Eq. (35)		polynomial bed, Eq. (36)	
m	1/3	1	1/3	1
C	7.624×10^6	7.208×10^{10}	7.624×10^6	7.208×10^{10}

Table 2: MISMIP 2D parameters. Unit for C is Pa m^{-m} s^m.

MISMIP experiments aim to model several steady state shapes that correspond to a given set of decreasing parameters $\{A_i, i = 1, ..., J\}$ for the ice softness, see [31]. The following procedure is applied to each experiment:

- **Initialize** the geometry with a ten-meter-thick ice sheet and ice shelf.
- **For** $i = 1, 2, ..., J-1, J, J-1, ..., 2, 1$, run the model with A_i as ice softness parameter until reaching a steady shape.

First, we use a constant thin layer of ice as an initial geometry and run the model with the highest parameter A_1 until reaching a steady shape. Then, A_i is set to the next smaller value such that the upper surface of ice transiently moves forward and stabilizes to an new shape, consistently with experiments a) and d) in Section 4.1. The position of the GL is recorded. This rule is repeated recursively until the lowest value of A_J. Then, the same procedure is run reversibly from the lowest value A_J to the highest one A_1. For all value of the set of A_i, the experiment provides one position of the advancing GL and one for the retreating GL. Like Section 4.1, the ice sheet is considered to be in a steady state when the normalized annual volume change is lower than 10^{-6}.

In practice, the SIA component of the velocity is negligible in the MISMIP experiments, the gradient of the top surface elevation remaining limited. As a

consequence, we do not account for the SIA component. Experiment 1a/2a is run three times with a Fixed Grid (FG) strategy of various resolutions ($\mathtt{h} \sim 7$ km, ~ 3.5 km and ~ 1.7 km) and once with an Adaptive Grid (AG) strategy, see Section 3.2.3. Experiments 1b/2b, 3a, and 3b are run with an AG strategy only. Adaptivity parameters are $\mathtt{h}_{\min} \sim 0.1$ km, $\mathtt{h}_{\max} \sim 14$ km and $L_f = 10$ km, i.e. the resolution close to the GL is ~ 100 meters and ~ 10 km otherwise.

To validate our results, we use the following analytic expression for the ice softness parameter A with respect to the GL position x_{GL}:

$$A(x_{GL}) = \left[4^n C (a x_{GL})^{m+1}\right] \Big/ \left[(\rho g)^{n+1} \left(1 - \frac{\rho}{\rho_w}\right)^n \left(-\frac{\rho_w}{\rho} b(x_{GL})\right)^{n+m+3} \right]. \tag{37}$$

This formula is derived from the boundary layer theory presented in [34], and is valid only for steady GLs.

Fig. 5 left (resp. right) displays the advancing (resp. retreating) steady state shapes reached when A is decreasing (resp. increasing) for experiments 1a/2a and 3a with an AG strategy. Experiment 1a/2a shows a regular advance of the GL for decreasing A and a quasi-symmetric retreat for re-increasing A. The reversibility of the GL is then verified in this case. As expected [34], this is no longer the case with experiment 3a since a depression occurs in the bedrock. Indeed, when the advancing GL reaches the upward-sloping part of the bed, it jumps to the next downward-sloping part. The same appends during the retreating stage.

Fig. 6 displays the ice softness A as a function of the GL position for several grid strategies and experiments. For the lowest mesh resolution in the experiment 1a/2a with FG strategy, the GL does not follow the advancing stages during retreating ones in a symmetric way. Indeed, when the parameter A re-increases, the GL remains stuck for a few stages before retreating. This delay was already observed in [39]. However, when using a finer mesh, the misfit between advancing and retreating positions decreases and the two phases get closer. Moreover, the GL positions converge to the analytic solution (37). Interestingly, retreating GL positions are closer to the solution than advancing ones for low mesh resolutions. This is also slightly visible when using an AG strategy. This indicates that a finer mesh is required to represent the advancing GL than the retreating one with the same accuracy. As observed earlier, the GL is reversible and fits the analytic solution when strongly refining the mesh close to the GL (AG). In contrast, the GL of experiment 1b/2b is slightly less reversible than for the experiment 1a/2a. Indeed, the linear-type basal sliding parametrization induces a sharper and narrower transition in the SSA velocity, such that an even more intensive refinement is needed to improve the GL reversibility. Moreover, as already observed the retreating GL is closer to the solution than the advancing one. An additional experiment (not shown) with a greater accuracy close to the GL ($\mathtt{h}_{\min} = 0.01$ km) shows indistinguishable advancing and retreating curves. As expected, the GL of experiment 3a displays a jump where the bed is upward-sloping and the retreating stage takes a different path. Both advancing and retreating positions fit perfectly the analytic solution

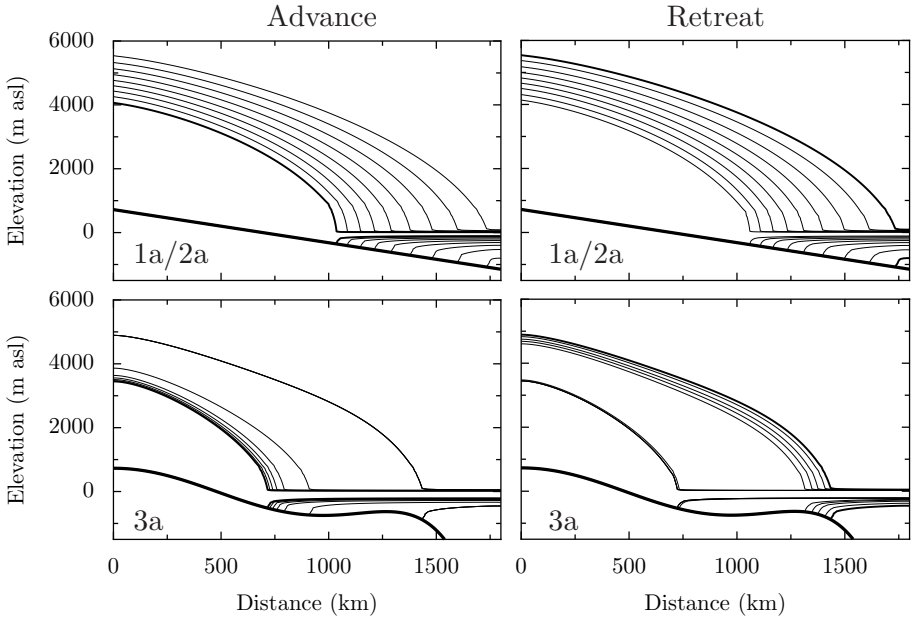

Figure 5: Advancing (left) and retreating (right) steady state shapes for experiments 1a/2a (top) and 3a (bottom) when using an AG strategy.

(37). Like experiment 1b/2b compared to 1a/2a, the GL of experiment 3b does not follow the analytic solution (37) as neatly as experiment 3a does, especially during the advancing stages. However, the misfit in experiment 3b can be reduced by further refining (to $\mathtt{h}_{\min} = 0.01$ km) in this transition zone as done for experiment 1b/2b.

4.3. MISMIP 3D

Two-dimensional ice sheets miss blustering effects on the Grounding Line (GL) that are induced by lateral stresses [13]. In order to capture these effects one has to include the second horizontal dimension. In this section, we report one of the MISMIP 3D [30] experiments that involves a three-dimensional ice sheet. In contrast to MISMIP 2D, MISMIP 3D aims to verify the reversibility of the GL under a perturbation in the sliding parametrization C.

Consider the horizontal domain $\Omega = [0, 800] \times [0, 50]$ km and a flat sloppy bedrock defined by $b(x, y) = -100 - x/1000$, see Fig. 7. We assume a constant accumulation rate $a = 0.5$ m a^{-1}, such that the presence of an upstream ice sheet and of a downstream ice shelf are guaranteed. Symmetry is imposed at $x = 0$ km while, at the ocean boundary of the ice shelf ($x = 800$ km), the ice pressure is balanced by the hydrostatic sea water pressure (condition (15)). Either a free-slip boundary condition or a free condition for the SSA (equations (12) (13)) occurs on the side $y = 0$ km (also called side A), while another free-slip boundary condition for the SSA occurs at $y = 50$ km (also called side B).

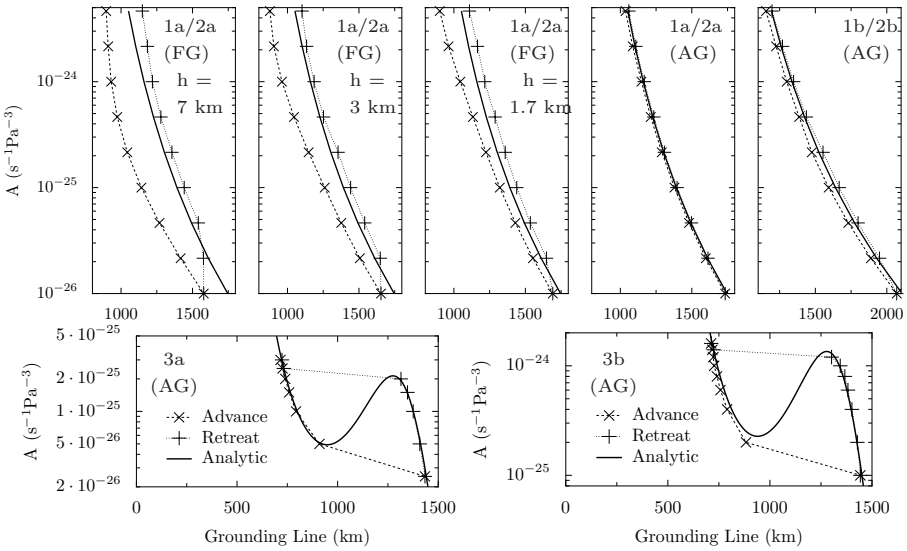

Figure 6: Parameter A with respect to the GL position when using FG and AG strategies. The analytic solution is drawn with the bold line from the formula (37).

As ice softness, we use the parameter $A = 4.6416 \times 10^{-26}$ Pa^{-3} s^{-1}, and as sliding law, we use $m = 1/3$ and

$$C(x,y) = \bar{C}\left[1 - \bar{a}\,\exp\left(-\frac{(x - x_{GL}(0))^2}{2\,(150\times 10^3)^2} - \frac{y^2}{2\,(10\times 10^3)^2}\right)\right], \qquad (38)$$

where $x_{GL}(y)$ is the x-coordinate of the GL at the ordinate y, $\bar{a} \geq 0$ is the perturbation amplitude and $\bar{C} = 7.624 \times 10^6$ Pa m$^{-1/3}$ s$^{1/3}$ [30]. When $\bar{a} = 0$, $C = \bar{C}$ is constant. When $\bar{a} > 0$, the sliding coefficient $C(x,y)$ contains a perturbation by a Gaussian function which is maximal at point $(x_{GL}(0), 0)$ of the GL (black point in Fig. 7).

The MISMIP 3D experiment consists of four steps, the model being transiently run with changing boundary and sliding conditions as indicated in Table 3. Like for MISMIP 2D, the ice geometry of step 1 is initialized by a ten-meter-thick layer of ice (grounded and floating) on Ω. Afterwards, the initial geometries of steps 2, 3 and 4 are taken from the last geometries obtained in steps 1, 2 and 3, respectively.

In step 1, we impose a free-slip condition on side A and apply a sliding condition without perturbation, i.e. $\bar{a} = 0$. In such configuration, the problem is symmetric in y, such that the two-dimensional model can be used. The model is run until a steady state shape is reached. In step 2, the boundary condition on side A is released into an entirely free condition. Since, the problem is no longer symmetric, we run the three-dimensional model until reaching a new steady state shape. In step 3, we apply a perturbation in the sliding condition by setting $\bar{a} = 0.75$ and running the model for 100 years. In step 4, we remove

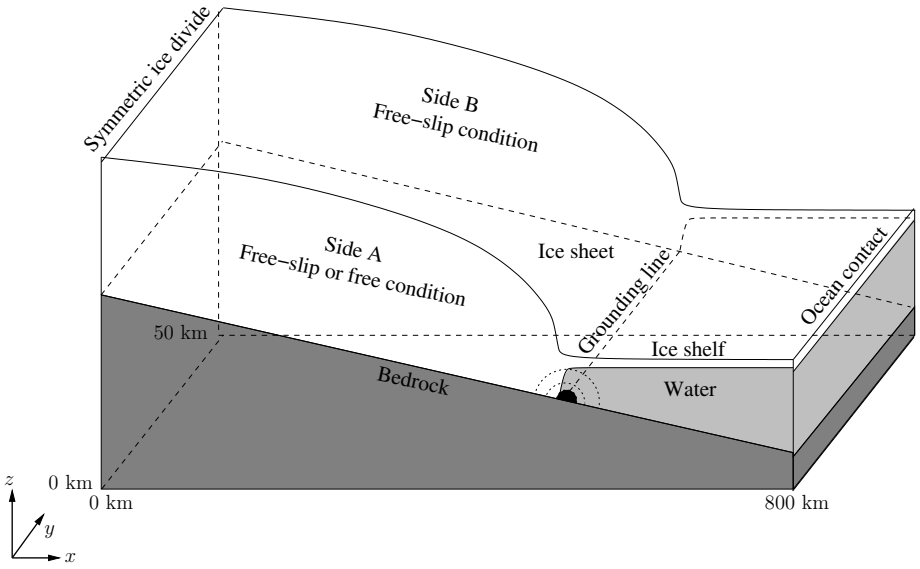

Figure 7: Set-up of the MISMIP 3D experiment. The black point corresponds to the place where the perturbation is maximal.

Step J	1	2	3	4
Condition on side A	free-slip	free		
$\bar{a}$	0		0.75	0
Simulation time	steady state	steady state	100 years	steady state
Model dimension	2	3		

Table 3: MISMIP 3D parametrization of boundary and sliding conditions for each one of the four steps.

the perturbation by setting $\bar{a} = 0$ and run the model until reaching a new steady state shape. The ice sheet is considered to be in a steady state when the normalized annual volume change is lower than 10^{-5} and when the annual GL position change on side A is lower than 1 m.

Like for MISMIP 2D, we only consider the SSA model since the SIA components of the velocity are negligible in the MISMIP 3D experiments, the gradients of the involved ice sheet surfaces being low. Steps 1-4 are performed with the two grid strategies, see Section 3.2.3. First, we use a regular Fixed Grid (FG) on Ω with $\mathtt{h} \sim 1.5$ km. Second, we use an Adaptive Grid (AG) with the parameters $\mathtt{h}_{\min} \sim 0.2$ km, $\mathtt{h}_{\max} \sim 6$ km and $L_f = 20$ km, i.e. the resolution close to the GL is 200 meters and 6 km elsewhere. For both AG and FG, the number of points of the mesh is comparable: $\sim 15\,000$.

The profiles of the ice sheets at time t_{S_J} – the last iteration of step J –

for $J = 1, 2, 3, 4$ are displayed in Fig. 8 when using an AG strategy. Table 4 displays the GL variations during step J on side A and B:

$$dx_{GL}^{A,J} := x_{GL}(y_A, t_{S_J}) - x_{GL}(y_A, t_{S_{J-1}}), \tag{39}$$

$$dx_{GL}^{B,J} := x_{GL}(y_B, t_{S_J}) - x_{GL}(y_B, t_{S_{J-1}}), \tag{40}$$

where $y_A = 0$ km and $y_B = 50$ km. Fig. 9 displays the x-velocity and y-velocity fields at time t_{S_2} (just before perturbation), t_{S_2+1} (just after perturbation), and t_{S_3} (just before removing the perturbation) using an AG strategy. Eventually, the evolutions of the GL after perturbation (step 3) and after removing the perturbation (step 4) are displayed on Fig. 10 for both FG and AG strategies.

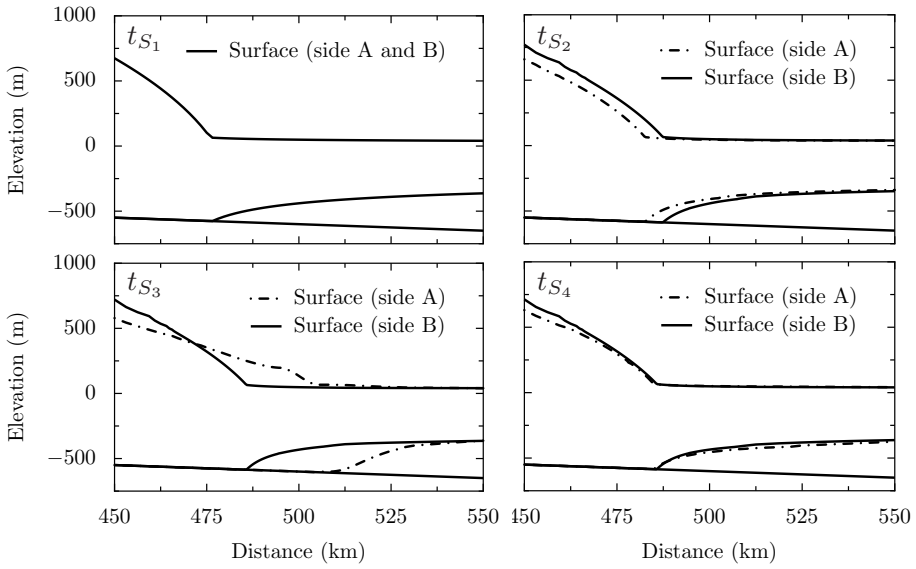

Figure 8: Upper and lower surfaces of the ice sheet at the end of steps 1, 2, 3 and 4 on side A (dashed-dotted line) and B (continuous line) with an AG strategy.

Step J	2		3		4		**3 + 4**	
Grid	FG	AG	FG	AG	FG	AG	**FG**	**AG**
$dx_{GL}^{A,J}$	0.9	7.5	40.8	22.1	-26.9	-19.7	**13.9**	**2.4**
$dx_{GL}^{B,J}$	4.2	12.2	5.4	-1.6	7	0	**12.4**	**-1.6**

Table 4: GL variations (unit: km) using an AG strategy during step J on sides A and B.

When using the AG strategy, the GL position stabilizes at ~ 475 km from the origin at the end of step 1. During step 2, the GL advances by ~ 7.5 km on side A and by ~ 12 km on side B. Indeed, lateral velocities (Fig. 9) appear after releasing the free-slip condition into an total-free condition on

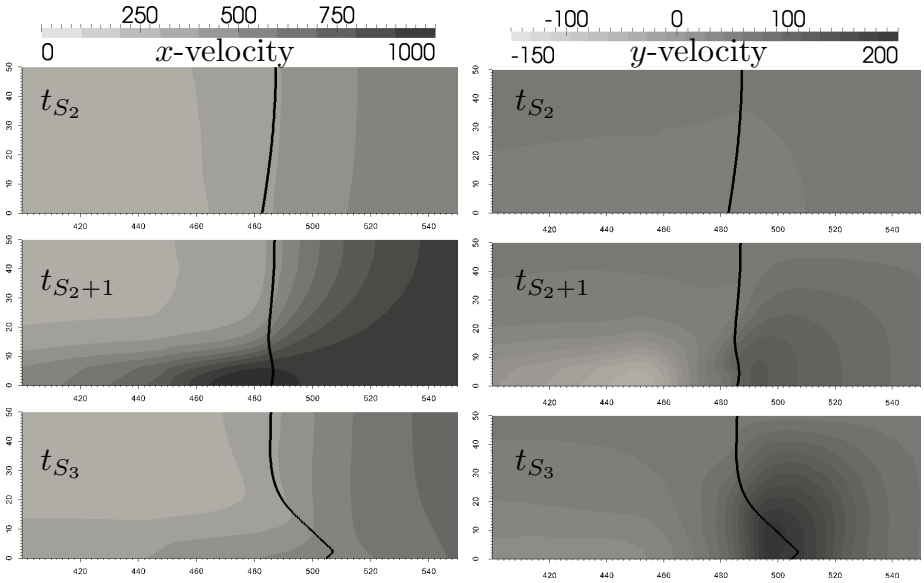

Figure 9: x-SSA-velocity (left) and y-SSA-velocity (right) fields sky view before perturbation (time t_{S_2}), just after perturbation (time t_{S_2+1}) and after 100 years (time t_{S_3}), respectively. The GL is drawn with the bold line.

side A. This generates a lateral flux and then reduces the flux of ice along the GL. As a consequence, the GL moves forward to compensate the excess of accumulation. This is even more pronounced on side B, where the flux is reduced the most. In step 3, the sliding perturbation substantially impacts the lateral and longitudinal velocities (Fig. 9). On side A, longitudinal velocities substantially amplify close to GL while the lateral velocities become negative upstream the GL (where the perturbation is maximal) and positive downstream. One hundred years later, the perturbed ice flow has moved the GL forward by ~ 22 km on side A and moved the GL backward by ~ 1.6 km on side B. Once the perturbation removed (in step 4), the GL on side A moves back almost to its original position, ~ 2.5 km in front of this one while the GL on side B almost does not move. We conclude that using an AG strategy allows us to reproduce a correct reversible GL.

The FG strategy shows significant differences in its effect on the GL position compared to the AG during steps 3 and 4. During step 3, the GL advances twice more: ~ 41 km on side A, and advances by ~ 5 km on side B while it slightly retreats when using an AG. In contrast with AG, the GL hardly recovers the position it had before the perturbation during step 4. Indeed, the difference between the GL positions exceeds 12 km from side A to side B. Like with MISMIP 2D, this underlines that the FG strategy can only reproduce a reversible GL if the number of unknowns is much larger compared to AG, making the FG strategy impractical for real world problems.

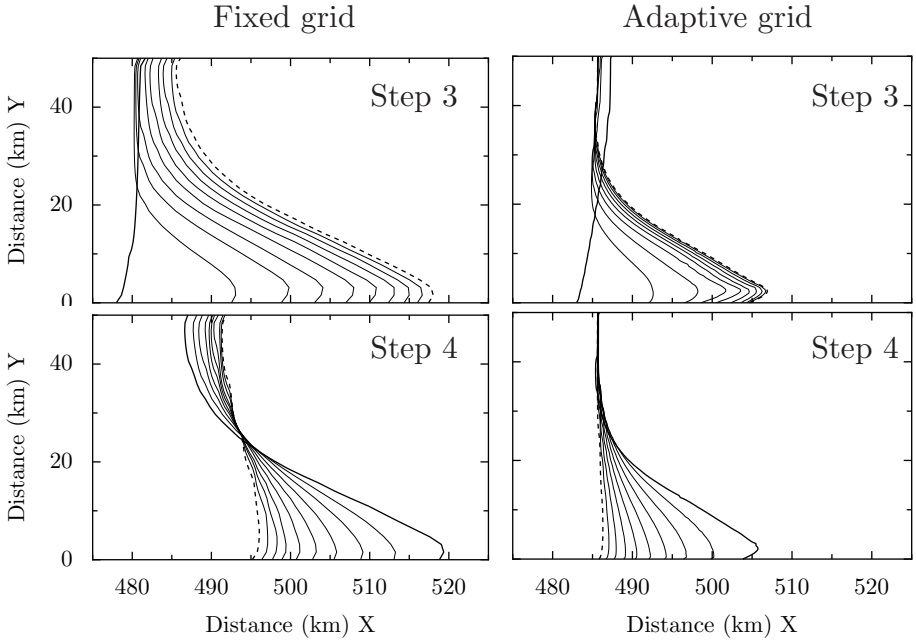

Figure 10: Evolution of the GL (sky view) during step 2 (advance, top) and step 3 (retreat, bottom) with FG (left) and AG (right) strategies. The bold lines correspond to the first ice geometry, continuous lines correspond to transient geometries every 10 years and the dashed lines correspond to the last geometry (after 100 years).

5. Perspectives

In all MISMIP experiments, adaptivity was found essential to reproduce the correct motion of the GL with reasonable computational cost. Using the reversibility of the GL as a criterion to assess the quality of the mesh, we found that $\sim$ 100-metre-large elements were needed in a 20 km large zone surrounding the GL zone, while $\sim$ 10-kilometre-large elements were enough outside this zone. Such numbers were found empirically and are expected to change when using different parameters. Ideally, an adaptivity procedure should be independent of any physical parameter. In particular, implementing residual or hierarchic *a posteriori* error estimators for the SSA equation, like the ones proposed in [1] and [41] respectively, might be one way to build more robust local refinement procedures. This issue will be addressed in a future work.

Our model is based on the linear superposition of a one-dimensional vertical model (SIA) and a two-dimensional horizontal model (SSA) to reconstruct the three-dimensional ice flow. Even if this superposition is physically justified for most of ice sheets and ice shelves [39], our model might miss local three-dimensional effects of the ice flow. Such effects can only be accounted for by a three-dimensional model like the First Order Approximation (FOA) [4]. Comparing "SIA + SSA" and FOA solutions would be of interest to confirm or

discount the validity of the linear superposition "SIA + SSA" for marine ice sheets.

As a long term perspective, our model aims to be applied to real ice sheets and ice shelves. For that, one needs to account for further physical aspects of ice sheets and ice shelves. First, one needs to model the ice temperature field and its two-way effects on the ice flow behaviour. Second, a parametrization of the bed yield stress with respect to the presence of basal water in the till [6] is highly desirable, but this would require an additional hydrological model. Third, a complete mass balance model needs to be advocated. This includes a sub-glacial and surfacial melting model, an ice accumulation model and a calving model that accounts for the formation of icebergs.

6. Acknowledgements

The authors thank Ralf Kornhuber for his support, Ed Bueler for helpful discussions and Maria Baden for English proofreading.

References

[1] J. Baranger and H. El Amri. Estimateurs a posteriori d'erreur pour le calcul adaptatif d'écoulements quasi-newtoniens. RAIRO - Modélisation mathématique et analyse numérique, 25:31–47, 1991.

[2] J. W. Barrett and W. B. Liu. Finite element approximation of the p-Laplacian. Mathematics of Computation, 61:523–537, 1993.

[3] R. Bermejo and J.A. Infante. A multigrid algorithm for the p-Laplacian. SIAM J. Sci. Comput., 21:1774–1789, December 1999.

[4] H. Blatter. Velocity and stress fields in grounded glaciers: a simple algorithm for including deviatoric stress gradients. J. Glaciol., 41(138):333–344, 1995.

[5] J. Brown, B. Smith, and A. Ahmadia. Achieving textbook multigrid efficiency for hydrostatic ice sheet flow. SIAM J. Scientific Computing. Accepted for publication.

[6] E. Bueler and J. Brown. Shallow shelf approximation as a "sliding law" in a thermomechanically coupled ice sheet model. Journal of Geophysical Research - Earth Surface, 114(F3):F03008+, July 2009.

[7] D. Docquier, L. Perichon, and F. Pattyn. Representing grounding line dynamics in numerical ice sheet models: Recent advances and outlook. Surveys in Geophysics, 32:417–435, 2011.

[8] G. Durand, O. Gagliardini, B. de Fleurian, T. Zwinger, and E. Le Meur. Marine ice sheet dynamics: Hysteresis and neutral equilibrium. Journal of Geophysical Research, 114, 2009.

[9] G. Durand, O. Gagliardini, T. Zwinger, E. Le Meur, and R. C.A. Hindmarsh. Full Stokes modeling of marine ice sheets: influence of the grid size. Annals of Glaciology, 50(52):109–114, 2009.

[10] D.L. Egholm and S.B. Nielsen. An adaptive finite volume solver for ice sheets and glaciers. Journal of Geophysical Research, 115:F01006, 2010.

[11] A. Ern and J.L. Guermond. Theory and practice of finite elements. Springer, 2004.

[12] R. Glowinski. Handbook of Numerical Analysis: Numerical Methods for Fluids (Part 3), volume 9. Elsevier Science Ltd, 2003.

[13] D. Goldberg, D. M. Holland, and C. Schoof. Grounding line movement and ice shelf buttressing in marine ice sheets. Journal of Geophysical Research, 114(F04026), 2009.

[14] C. Gräser. Convex Minimization and Phase Field Models. PhD thesis, FU Berlin, 2011.

[15] C. Gräser and R. Kornhuber. Multigrid methods for obstacle problems. Journal of Computational Mathematics, 27(1):1–44, 2009.

[16] C. Gräser, U. Sack, and O. Sander. Truncated nonsmooth Newton multigrid methods for convex minimization problems. In Domain Decomposition Methods in Science and Engineering XVIII, volume 70 of Lecture Notes in Computational Science and Engineering, pages 129–136. Springer Berlin Heidelberg, 2009.

[17] C. Gräser and O. Sander. The dune-subgrid module and some applications. Computing, 86(4):269–290, 2009.

[18] C. Gräser and O. Sander. Polyhedral Gauß–Seidel converges. Preprint 696, Matheon, 2010.

[19] R. Greve and H. Blatter. Dynamics of Ice Sheets and Glaciers. Springer Verlag, 2009.

[20] W. Hackbusch. Multi-grid methods and applications. Springer series in computational mathematics. Springer, 1985.

[21] Y. Q. Huang, R. Li, and W. Liu. Preconditioned descent algorithms for p-Laplacian. J. Sci. Comput., 32:343–371, August 2007.

[22] I. Joughin and R. B. Alley. Stability of the west antarctic ice sheet in a warming world. Nature Geoscience, 4:506–513, 2011.

[23] G. Jouvet and E. Bueler. Steady, shallow ice sheets as obstacle problems: well-posedness and finite element approximation. SIAM J. Appl. Math., 72(4):1292–1314, 2012.

[24] G. Jouvet, E. Bueler, C. Gräser, and R. Kornhuber. A nonsmooth Newton multigrid method for a hybrid, shallow model of marine ice sheets. 8th International Conference on Scientific Computing and Applications. AMS, 2012.

[25] R. Kornhuber. Monotone multigrid methods for elliptic variational inequalities. I. Numer. Math., 69(2):167–184, 1994.

[26] R. Kornhuber. Nonlinear multigrid techniques. 'Theory and Numerics of Differential Equations', Springer., pages 179–229, 2001.

[27] R. J. Leveque. Finite Volume Methods for Hyperbolic Problems. Cambridge Univ. Press, 2002.

[28] W. S. B. Paterson. The Physics of Glaciers. Pergamon, 3rd edition, 1994.

[29] F. Pattyn, A. Huyghe, S. De Brabander, and B. De Smedt. Role of transition zones in marine ice sheet dynamics. Journal of Geophysical Research, 111(F2):1–10, 2006.

[30] F. Pattyn, Perichon L., Durand G., Favier L., Gagliardini O., Hindmarsh R. C. A., Zwinger T., Albrecht T., Cornford S., Docquier D., Furst J. J., Goldberg D., Gudmundsson H., Humbert A., Hutten M., Huybrechts P., Jouvet G., Kleiner T., Larour E., Martin D., Morlighen M., Payne A. J., Pollard D., Ruckamp M., Rybak O., Seroussi E., Thoma M., and Wilkens N. Grounding-line migration in plan-view marine ice-sheet models: results of the ice2sea MISMIP3d intercomparison. Accepted for publication in Journal of Glaciology, 2012.

[31] F. Pattyn, C. Schoof, L. Perichon, R. C. A. Hindmarsh, E. Bueler, B. de Fleurian, G. Durand, O. Gagliardini, R. Gladstone, D. Goldberg, G. H. Gudmundsson, V. Lee, F. M. Nick, A. J. Payne, D. Pollard, O. Rybak, F. Saito, and A. Vieli. Results of the marine ice sheet model intercomparison project, MISMIP. The Cryosphere Discussions, 6(1):267–308, 2012.

[32] C. Raymond. Deformation in the vicinity of divides. Journal of Glaciology, 34:357–373, 1983.

[33] C. Schoof. Variational methods for glacier flow over plastic till. J. Fluid Mech., 555:299–320, 2006.

[34] C. Schoof. Ice sheet grounding line dynamics: Steady states, stability, and hysteresis. Journal of Geophysical Research, 112(F3):F03S28+, July 2007.

[35] C. Schoof. Coulomb friction and other sliding laws in a higher order glacier flow model. Mathematical Models and Methods in Applied Sciences, 2009.

[36] J. Stoer and R. Bulirsch. Introduction to Numerical Analysis. Springer, Berlin, New York, 3. edition, 2002.

[37] I. Velicogna and J. Wahr. Measurements of time-variable gravity show mass loss in antarctica. Science, 311(5768):1754–1756, 2006.

[38] A. Vieli and A. J. Payne. Assessing the ability of numerical ice sheet models to simulate grounding line migration. Journal of Geophysical Research, 110(F1):1–18, 2005.

[39] R. Winkelmann, M. A. Martin, M. Haseloff, T. Albrecht, E. Bueler, C. Khroulev, and A. Levermann. The Potsdam Parallel Ice Sheet Model (PISM-PIK) Part 1: Model description. The Cryosphere, 5:715–726, 2011.

[40] J. Xu. The method of subspace corrections. J. Comput. Appl. Math., 128(1-2):335–362, 2001. Numerical analysis 2000, Vol. VII, Partial differential equations.

[41] Q. Zou, A. Veeser, R. Kornhuber, and C. Gräser. Hierarchical error estimates for the energy functional in obstacle problems. Numer. Math., 117:653–677, 2011.